Journal of Applied Mathematics and Computational Mechanics 2022, 21(2), 63-76
www.amcm.pcz.pl p-ISSN 2299-9965
DOI: 10.17512/jamcm.2022.2.06 e-ISSN 2353-0588

THERMO-DIFFUSION MHD CONVECTION IN ENCLOSURE USING HEAT AND MASS LINES VISUALIZATION TECHNIQUES

***Durgesh Kushawaha*[1], *Sushil Yadav*[2], *Dwesh K. Singh*[3], *Pravata Kumar Behera*[4]**

[1] *Department of Mathematics, Kalindi College, University of Delhi, Delhi, India*
[2] *Department of Mathematics, Maharaja Agrasen College, University of Delhi, Delhi, India*
[3] *Department of Mechanical Engineering, Dr. B.R. Ambedkar National Institute of Technology Jalandhar, India*
[4] *Department of Physics, ARSD College, University of Delhi, Delhi, India*
durgeshoct@gmail.com, syadav@mac.du.ac.in, singhdk@nitj.ac.in, pravat.arsd@gmail.com

Received: 15 December 2021; Accepted: 15 May 2022

Abstract. The numerical study of two-dimensional laminar thermo-diffusion natural convection in an exponentially heated and concentrated square enclosure of unit length in the presence of a uniform horizontal magnetic field is presented in this paper. The left and right vertical walls are assumed to have higher and lower temperatures and concentrations, respectively, and are governed by exponential functions, whereas the horizontal walls are assumed to be adiabatic and non-diffusive. The mathematical formulation of heat and mass functions has been completed, and heat and mass line contours have been drawn based on these functions to investigate the behavior of heat and mass in the cavity. The flow governing equations were solved using a finite difference method in conjunction with the Successive Over-Relaxation (SOR) technique and then converted to a vorticity-stream function form. A detailed comparison of isotherms with heatlines and isosolutes with masslines has been performed. Furthermore, the reduction for lower Rayleigh numbers Ra surpassing the reduction for higher values of Ra. The maximum reduction in overall heat and mass transfer has been observed for higher Hartmann $(\mathrm{Ha} = 8)$.

MSC 2010: *35Q30, 76M20, 80A20, 76W05, 82D15, 82D80*
Keywords: *thermo-diffusion, heatlines, masslines, magnetic field, overall heat and mass transfer*

Nomenclature

English letters

β_{S^*}	solute expansion coefficient
β_{T^*}	thermal expansion coefficient
(U,V)	dimensionless velocity components
(u,v)	dimensional velocity components $\left[\mathrm{ms}^{-1}\right]$
(X,Y)	dimensionless coordinates
(x,y)	dimensional coordinates $[\mathrm{m}]$
Nu	Nusselt number
Sh	Sherwood number
g	gravitational acceleration $\left[\mathrm{ms}^{-2}\right]$
B	magnetic field strength
D	mass diffusivity $\left[\mathrm{m}^2\mathrm{s}^{-1}\right]$
H	dimensionless heat function

h	dimensional heat function
J	heat flux
L	enclosure side
M	dimensionless mass function
m	dimensional mass function
N	buoyancy ratio
P	dimensionless pressure
p	dimesional pressure $\left[\mathrm{Nm}^{-2}\right]$
S	dimensionless solute
S^*	dimensional solute $\left[\mathrm{Kgm}^{-3}\right]$
T	dimensionless temperature
T^*	dimensional temperature [K]
Greek symbols	
α	thermal diffusivity $\left[\mathrm{m}^2\mathrm{s}^{-1}\right]$
μ	dynamic viscosity $\left[\mathrm{Kgm}^{-1}\mathrm{s}^{-1}\right]$
ν	kinematic viscosity $\left[\mathrm{m}^2\mathrm{s}^{-1}\right]$
Ω	dimensionless vorticity
ω	dimensional vorticity
ρ	fluid density $\left[\mathrm{Kgm}^{-3}\right]$
σ	electrical conductivity $\left[\mathrm{Wm}^{-1}\mathrm{K}^{-1}\right]$
k	thermal conductivity $\left[\mathrm{Wm}^{-1}\mathrm{K}^{-1}\right]$
Subscripts	
avg	average
min	maximum
min	minimum
h	higher
l	lower

1. Introduction

The process of thermo-diffusion natural convection is governed by the combined temperature and concentration gradients. The most recent works [1–4] show that isotherms, isoconcentration, and streamlines are frequently used to investigate the thermo-diffusion natural convection phenomenon. The streamlines visualization technique effectively depicts fluid flow. The isotherms and isoconcentrations are used to visualize the heat and mass flows within the domain, but they cannot represent the 'heat flow' and 'mass flow' because the isotherms and isoconcentrations only indicate the spatial distribution of temperature and concentration. Understanding the heat and mass flow during thermo-diffusion convection requires a visualization tool similar to streamlines. As a result, we use the heat and mass lines techniques to fully visualize 'heat flow' and 'mass flow,' respectively. Only a few authors have used heat and mass lines techniques to fully visualize heat and mass flows in cavities. We've listed a few of them here where the authors used the aforementioned visualization techniques. The visualization tools for heat and mass lines were used in [5–7]. Some very important contributions have been done by Prof. Sohail A. Khan and his group members in the numerical investigation of heat transfer with entropy generation minimization [8–11] in various types of nanofluids in numerous types of geometries. Furthermore, they have also investigated double-diffusion in Sisko fluid flow with variable properties [12], heat transfer and entropy analysis using liquid hydrogen based nanoliquid [13] and mixed convection utilizing CNTs [14,15] as well as Ree-Eyring nanofluid flow with entropy generation analysis [16].

2. Problem formulation

The current study's problem formulation is divided into two parts: the physical model is explained in the first part, and the mathematical formulation is presented in the second part.

2.1. Physical model

The current work considers steady, laminar, and incompressible flow in a square enclosure, as shown in Figure 1. Water, a Newtonian fluid, has been considered as the working fluid $(\mathrm{Pr} = 6.2)$. The left wall is kept at a higher temperature and solute concentration, while the right wall is kept at a lower temperature and solute concentration. Along the horizontal walls, heat and mass transmissions are adiabatic. No-slip velocity boundary conditions, i.e., $u = v = 0$, apply to all solid walls. A uniform magnetic field of strength B is applied in the x-direction.

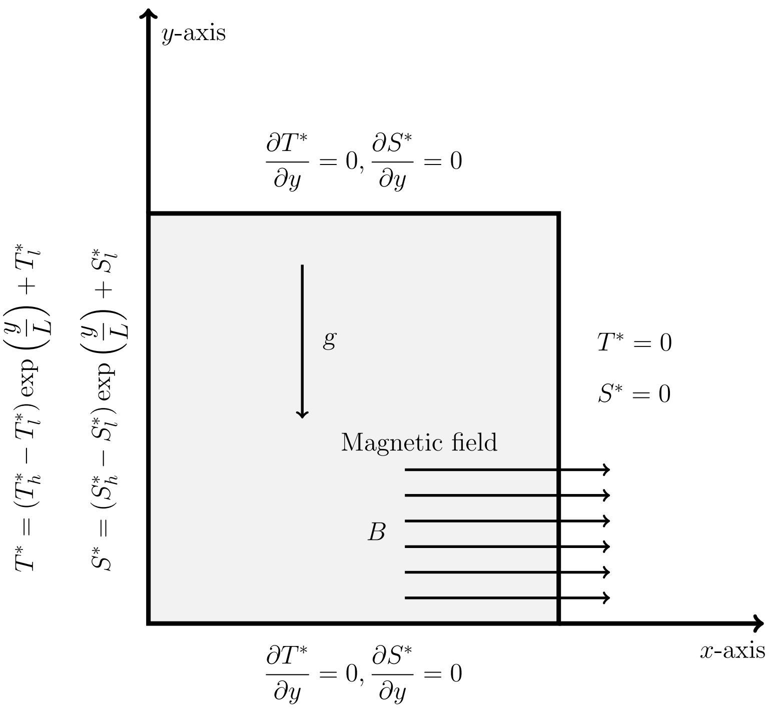

Fig. 1. The physical model of the problem under consideration

2.2. Mathematical formulation

The current study's mathematical formulation was derived from a physical model that included flow controlling equations in dimensional and non-dimensional forms, as well as boundary conditions. In addition, the dimensional and non-dimensional forms of steam, heat, and mass functions are addressed. The flow governing equations which are continuity, momentum, energy, and solute transfer equations in dimensional form are as follows [7]:

$$\frac{\partial u}{\partial x}+\frac{\partial v}{\partial y}=0, \tag{1}$$

$$\rho\left(u\frac{\partial u}{\partial x}+v\frac{\partial u}{\partial y}\right)=-\frac{\partial p}{\partial x}+\mu\left(\frac{\partial^2 u}{\partial x^2}+\frac{\partial^2 u}{\partial y^2}\right), \tag{2}$$

$$\begin{aligned}\rho\left(u\frac{\partial v}{\partial x}+v\frac{\partial v}{\partial y}\right)=-\frac{\partial p}{\partial y}+\mu\left(\frac{\partial^2 v}{\partial x^2}+\frac{\partial^2 v}{\partial y^2}\right)+(\rho\beta_{T^*})\,g\,(T^*-T_l^*)\\ +(\rho\beta_{S^*})\,g\,(S^*-S_l^*)-\sigma B^2 v,\end{aligned} \tag{3}$$

$$(\rho c_p)\left(u\frac{\partial T^*}{\partial x}+v\frac{\partial T^*}{\partial y}\right)=k\left(\frac{\partial^2 T^*}{\partial x^2}+\frac{\partial^2 T^*}{\partial y^2}\right), \tag{4}$$

$$u\frac{\partial S^*}{\partial x}+v\frac{\partial S^*}{\partial y}=D\left(\frac{\partial^2 S^*}{\partial x^2}+\frac{\partial^2 S^*}{\partial y^2}\right). \tag{5}$$

Using stream function $\left(u=\frac{\partial\psi}{\partial y}, v=-\frac{\partial\psi}{\partial x}\right)$, vorticity $\left(\omega=\frac{\partial v}{\partial x}-\frac{\partial u}{\partial y}\right)$ transformation alone with the following non-dimensional parameters

$$\begin{gathered}X=\frac{x}{L},\quad Y=\frac{y}{L},\quad U=\frac{uL}{\alpha_f},\quad V=\frac{vL}{\alpha},\quad \Psi=\frac{\psi}{\alpha},\quad P=\frac{pL^2}{\rho\,\alpha^2}\\ \mathrm{Pr}=\frac{\nu}{\alpha},\quad \mathrm{Le}=\frac{\alpha}{D},\quad \Omega=\frac{\omega L^2}{\alpha},\quad T=\frac{T^*-T_l^*}{T_h^*-T_l^*},\quad S=\frac{S^*-S_l^*}{S_h^*-S_l^*}\\ \mathrm{Ra}=\frac{g\beta_{T^*}\left(T_h^*-T_l^*\right)L^3}{\nu\alpha},\quad \mathrm{N}=\frac{(\rho\beta_{S^*})\left(S_h^*-S_l^*\right)}{(\rho\beta_{T^*})\left(T_h^*-T_l^*\right)},\quad \mathrm{Ha}=BL\sqrt{\frac{\sigma}{\mu}},\end{gathered} \tag{6}$$

the non-dimensional form of Eqs. (1) to (5) in stream function, vorticity, temperature, and solute equations are as follows:

$$\frac{\partial^2\Psi}{\partial X^2}+\frac{\partial^2\Psi}{\partial Y^2}=-\Omega \tag{7}$$

$$U\frac{\partial\Omega}{\partial X}+V\frac{\partial\Omega}{\partial Y}=\mathrm{Pr}\left(\frac{\partial^2\Omega}{\partial X^2}+\frac{\partial^2\Omega}{\partial Y^2}\right)+\mathrm{Ra}\,\mathrm{Pr}\left(\frac{\partial T}{\partial X}+\mathrm{N}\frac{\partial S}{\partial X}\right)-\mathrm{Ha}^2\,\mathrm{Pr}\frac{\partial V}{\partial X}, \tag{8}$$

$$U\frac{\partial T}{\partial X}+V\frac{\partial T}{\partial Y}=\frac{\partial^2 T}{\partial X^2}+\frac{\partial^2 T}{\partial Y^2}, \tag{9}$$

$$U\frac{\partial S}{\partial X}+V\frac{\partial S}{\partial Y}=\frac{1}{\mathrm{Le}}\left(\frac{\partial^2 S}{\partial X^2}+\frac{\partial^2 S}{\partial Y^2}\right), \tag{10}$$

The following are the non-dimensional boundary conditions for the non-dimensional flow governing Eqs. (7) to (10) [17, 18]:

$$\begin{aligned}
&\Psi=0,\ \Omega=-\frac{\partial^2\Psi}{\partial Y^2},\quad \frac{\partial T}{\partial Y}=\frac{\partial S}{\partial Y}=0,\ \text{along horizontal walls,}\\
&\Psi=0,\ \Omega=-\frac{\partial^2\Psi}{\partial X^2},\quad T=S=0,\ \text{along the right wall,}\\
&\Psi=0,\ \Omega=-\frac{\partial^2\Psi}{\partial X^2},\quad T=S=\exp(Y),\ \text{along the left wall.}
\end{aligned} \tag{11}$$

2.2.1. Stream function (Streamlines)

The non-dimensional stream function (Ψ) that governs the flow structure is defined as follows:

$$U=\frac{\partial \Psi}{\partial Y}\quad\text{and}\quad V=-\frac{\partial \Psi}{\partial X} \tag{12}$$

After manipulation, Eq. (12) can be rewritten as follows:

$$\frac{\partial^2\Psi}{\partial X^2}+\frac{\partial^2\Psi}{\partial Y^2}=\frac{\partial U}{\partial Y}-\frac{\partial V}{\partial X}. \tag{13}$$

Equation (13) is Poisson's equation for the non-dimensional stream function Ψ with source term $\frac{\partial U}{\partial Y}-\frac{\partial V}{\partial X}$. The solution to Eq. (13) yields the non-dimensional stream function, $\Psi(X,Y)$, and sketching isolines of this yields streamlines inside the enclosure.

2.2.2. Heat function (Heatlines)

The total heat flux vector, $\overrightarrow{J}=\left(J_x\overrightarrow{i}+J_y\overrightarrow{j}\right)$, containing the diffusion and convection transport, in x and y directions can be written as

$$J_x=(\rho c_p)\,u\,(T^*-T_l^*)-k\frac{\partial T^*}{\partial x},\quad J_y=(\rho c_p)\,v\,(T^*-T_l^*)-k\frac{\partial T^*}{\partial y} \tag{14}$$

$$\frac{\partial J_x}{\partial x} + \frac{\partial J_y}{\partial y} = (\rho c_p)\left(\frac{\partial uT^*}{\partial x} + \frac{\partial vT^*}{\partial y}\right) - k\left(\frac{\partial^2 T*}{\partial x^2} + \frac{\partial^2 T*}{\partial y^2}\right) = 0 \tag{15}$$

The dimensional heat function can be expressed in a differential form by treating h as a continuous scalar function [19, 20]:

$$-\frac{\partial h}{\partial x} = J_y, \quad \frac{\partial h}{\partial y} = J_x \tag{16}$$

Therefore, from Eq. (14) we have

$$-\frac{\partial h}{\partial x} = (\rho c_p)\, v\,(T^* - T_l^*) - k\frac{\partial T^*}{\partial y} \tag{17}$$

$$\frac{\partial h}{\partial y} = (\rho c_p)\, u\,(T^* - T_l^*) - k\frac{\partial T^*}{\partial x} \tag{18}$$

Using the non-dimensional parameters described in Eq. (6), we may express Eqs. (17) and (18) in the dimensionless form as follows:

$$-\frac{\partial H}{\partial X} = VT - \frac{\partial T}{\partial Y} \tag{19}$$

$$\frac{\partial H}{\partial Y} = UT - \frac{\partial T}{\partial X} \tag{20}$$

where H stands for the dimensionless heat function and is written as

$$H = \frac{h}{k\left(T_h^* - T_l^*\right)} \tag{21}$$

The manipulation of Eqs. (19) and (20) yields the following partial differential equation for the heat function.

$$\frac{\partial^2 H}{\partial X^2} + \frac{\partial^2 H}{\partial Y^2} = \frac{\partial\,(UT)}{\partial Y} - \frac{\partial\,(VT)}{\partial X} \tag{22}$$

By solving either Eq. (19), Eq. (20), or Eq. (22), we can obtain the dimensionless heat function H in the inner region of the rectangular enclosure under consideration. Heatlines are created by creating isolines with the heat function.

The following are the corresponding boundary conditions for the heat function H:

$$\begin{aligned}
&\text{for,} \quad X = 0 \quad \text{and} \quad X = 1, \quad \frac{\partial H}{\partial X} = 0,\\
&\text{for,} \quad Y = 0, \quad H = 0,\\
&\text{for,} \quad Y = 1, \quad H = \mathrm{Nu}_{\mathrm{avg}},
\end{aligned} \tag{23}$$

where $\mathrm{Nu}_{\mathrm{avg}}$ is given by

$$\mathrm{Nu}_{\mathrm{avg}} = \int_0^1 \mathrm{Nu}\, \mathrm{d}Y \tag{24}$$

and

$$\mathrm{Nu} = -\left.\frac{\partial T}{\partial X}\right|_{X=0}. \tag{25}$$

2.2.3. Mass function (Masslines)

In the dimensional form, the mass function [20,21] is given as m and defined as

$$-\frac{\partial m}{\partial x} = \rho v\left(S^* - S_l^*\right) - \rho D\frac{\partial S^*}{\partial y} \tag{26}$$

$$\frac{\partial m}{\partial y} = \rho u\left(S^* - S_l^*\right) - \rho D\frac{\partial S^*}{\partial x} \tag{27}$$

Using the non-dimensional parameters described in Eq. (6), we may express Eqs. (26) and (27) in the dimensionless form as follows:

$$-\frac{\partial M}{\partial X} = VS - \frac{1}{\mathrm{Le}}\frac{\partial S}{\partial Y} \tag{28}$$

$$\frac{\partial M}{\partial Y} = US - \frac{1}{\mathrm{Le}}\frac{\partial S}{\partial X} \tag{29}$$

where M is the non-dimensional mass function, which has the following definition:

$$M = \frac{m}{\mathrm{Le}\,\rho D\left(S_h^* - S_l^*\right)} \tag{30}$$

The following partial differential equation for the mass function is obtained by manipulating Eqs. (28) and (29).

$$\frac{\partial^2 M}{\partial X^2} + \frac{\partial^2 M}{\partial Y^2} = \frac{\partial\,(US)}{\partial Y} - \frac{\partial\,(VS)}{\partial X} \tag{31}$$

By solving either Eq. (28), Eq. (29), or Eq. (31), we can obtain the dimensionless mass function M in the inner region of the rectangular enclosure under consideration. Masslines are created by drawing isolines of the mass function.

The following are the equivalent boundary conditions for the mass function M:

$$
\begin{aligned}
&\text{for,} \quad X=0 \quad \text{and} \quad X=1, \quad \frac{\partial M}{\partial X}=0,\\
&\text{for,} \quad Y=0, \quad M=0,\\
&\text{for,} \quad Y=1, \quad M=\mathrm{Sh}_{\mathrm{avg}},
\end{aligned}
\tag{32}
$$

where $\mathrm{Sh}_{\mathrm{avg}}$ is given by

$$
\mathrm{Sh}_{\mathrm{avg}}=\int_0^1 \mathrm{Sh}\, \mathrm{d}Y \tag{33}
$$

and

$$
\mathrm{Sh}=-\left.\frac{\partial S}{\partial X}\right|_{X=0}. \tag{34}
$$

3. Solution methodology

The flow governing equations are solved using the procedures below:

Step 1: The finite difference method is used to discretize the governing Eqs. (7) to (10).

Step 2: Iteratively solve the collection of discretized governing equations.

Step 3: To compute the vorticity field in the computational domain, the vorticity equation Eq. (8) is solved first.

Step 4: The stream function equation Eq. (7) is then solved using the Successive Over-Relaxation (SOR) method, and the velocity values are obtained after we have the stream function field.

Step 5: The set of discretized equations for energy Eq. (9) and solute Eq. (10) transports in the computational domain are solved at the same time and utilize the new velocity values.

Step 6: The algebraic equations obtained following the discretization procedure are solved using in-house computer code written in FORTRAN-95.

Step 7: All dependent variables are assumed to be converged during the calculations if, and only if,

$$
\left|\chi_{i,j}^{n+1}-\chi_{i,j}^{n}\right| \leq 10^{-7}, \tag{35}
$$

where $\chi=(U,V,\Psi,\Omega,T,S)$, and (i,j) is the computation node point, and n is the iteration number.

4. Results and discussion

Figures 2 and 3 represent the effect of Rayleigh (Ra) and Hartmann (Ha) numbers on isotherms and heatlines. The top rows of both Figures 2 and 3 illustrate the isotherms for various Hartmann numbers $(0 \leq \mathrm{Ha} \leq 8)$. Even a minor increase in Ha causes a reduction in the temperature gradients on the vertical walls, resulting in the convection process dominated by conduction. The physics behind this is that electromagnetic force dominates the buoyancy force. It can also be noted that temperature gradients along the vertical walls rise as Ra strengthens from 5×10^3 to 5×10^4. The reason behind this is that buoyancy force dominates viscous force, therefore the convection process enhances subsequently. It can also be observed that isotherms only represent spatial distribution of temperature along a particular isotherm line. Therefore, isotherms are unable to visualize the heat flow inside the enclosure and hence heatlines are required to do the task. The bottom rows of both Figures 2 and 3 illustrate the heatlines for various Hartmann numbers $(0 \leq \mathrm{Ha} \leq 8)$. Each heatline contour has two types of lines: one of these are starting from a higher temperature wall and reaches at lower temperature wall and has positive intensity and responsible for direct heat transfer whereas other heatlines form a loop and have negative intensity and are responsible for thermal mixing. In this way heatlines help in completing the visualization of heat flow. Futhermore, the direct heat transfer and thermal mixing are denoted by H_{max} and H_{min}. From Figures 2 and 3 and Table 1, as Ra increases from 5×10^3 to 5×10^4, both H_{max} and H_{min} enhance. Subsequently, direct heat transfer and thermal mixing strengthen and hence significantly enhance in the convection process. However, magnitude of H_{max} dominates the magnitude H_{min} and hence thermal mixing is dominated by direct heat transfer. Furthermore, as Ha increases from 0 to 8, both the thermal mixing and direct heat transfer falls, but this fall is more for a lower Rayleigh number (Ra) in comparison to a higher Ra, and hence magnetic field is more effective for a lower Ra.

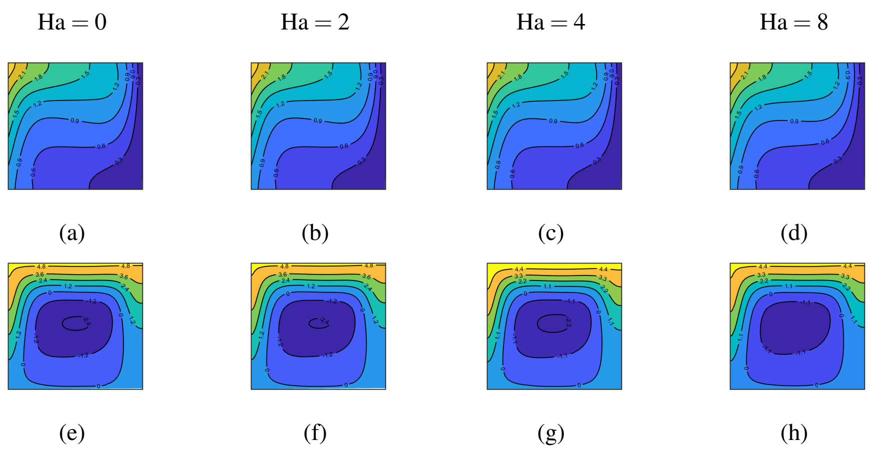

Fig. 2. Comparison of isotherms (T) (top row) and heatlines (H) (bottom row) for various Hartmann numbers (Ha) at $\mathrm{Ra} = 5 \times 10^3$, $\mathrm{Le} = 1$, and $\mathrm{N} = 1$

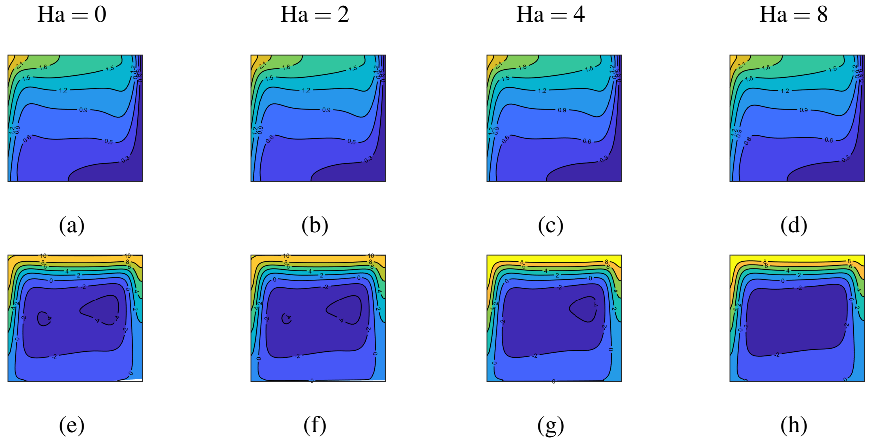

Fig. 3. Comparison of isotherms (T) (top row) and heatlines (H) (bottom row) for various Hartmann numbers (Ha) at $\mathrm{Ra} = 5 \times 10^4$, $\mathrm{Le} = 1$, and $\mathrm{N} = 1$

Table 1. Comparison of thermal mixing and direct heat transfer

Ha	$H_{\min}$	% change in $H_{\min}$	$H_{\max}$	% change in $H_{\max}$
		$\mathrm{Ra} = 5 \times 10^3$		
0	−2.477		4.955	
2	−2.437	1.61	4.927	0.57
4	−2.325	4.60	4.845	1.66
8	−1.975	15.05	4.555	5.99
		$\mathrm{Ra} = 5 \times 10^4$		
0	−4.454		10.063	
2	−4.420	0.76	10.043	0.20
4	−4.325	2.15	9.983	0.59
8	−3.994	7.65	9.756	2.27

Figures 4 and 5 represent the effect of Rayleigh (Ra) and Hartmann (Ha) numbers on isoconcentrations and masslines. The top rows of both Figures 4 and 5 illustrate the isoconcentrations for various Hartmann numbers $(0 \leq \mathrm{Ha} \leq 8)$. Even a minor increase in Ha causes a reduction in the concentration gradients on the vertical walls, resulting in the convection process dominated by conduction. The physics behind this is that electromagnetic force dominates the concentration buoyancy force. It can also be noted that concentration gradients along the vertical walls rise as Ra is strengthened from 5×10^3 to 5×10^4. The reason behind this is that concentration buoyancy force dominates viscous force, therefore convection process enhances subsequently. It can also be observed that isoconcentrations only represent spatial distribution of concentration along a particular isoconcentration line. Therefore, isoconcentrations are unable to visualize the mass flow inside the enclosure and hence masslines are required to do the task. The bottom rows of both Figures 4 and 5 illustrate the masslines for various Hartmann numbers $(0 \leq \mathrm{Ha} \leq 8)$.

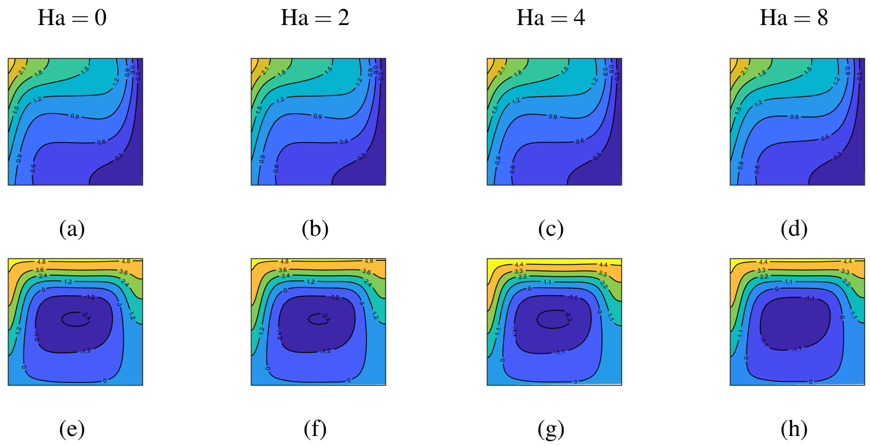

Fig. 4. Comparison of isoconcentration (S) (top row) and masslines (M) (bottom row) for various Hartmann numbers (Ha) at $\mathrm{Ra} = 5 \times 10^3$, $\mathrm{Le} = 1$, and $\mathrm{N} = 1$

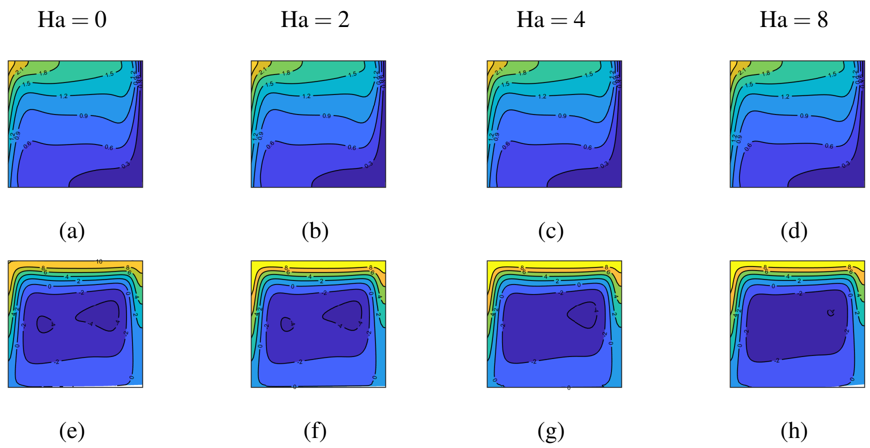

Fig. 5. Comparison of isoconcentration (S) (top row) and masslines (M) (bottom row) for various Hartmann numbers (Ha) at $\mathrm{Ra} = 5 \times 10^4$, $\mathrm{Le} = 1$, and $\mathrm{N} = 1$

Each massline contour has two types of lines: one of these are starting from higher concentration wall and reaches at a lower concentration wall and has positive intensity and responsible for direct mass transfer whereas other masslines form a loop and have negative intensity and are responsible for solute mixing. In this way masslines help in the complete visualizing of mass flow. Furthermore, the direct mass transfer and solute mixing are denoted by $M_{\max}$ and $M_{\min}$. From Figures 4 and 5, as Ra increases from 5×10^3 to 5×10^4, both $M_{\max}$ and $M_{\min}$ enhance. Subsequently, direct mass transfer and solute mixing strengthen and hence significantly enhance in convection process. But magnitude of $M_{\max}$ dominates the magnitude $M_{\min}$ and hence solute mixing is dominated by direct mass transfer. Furthermore, as Ha increases from 0 to 8, both the solute mixing and direct mass transfer falls but this fall is more for lower Rayleigh number (Ra) in comparison to higher Ra and hence magnetic field is more effective for lower Ra.

Table 2. Comparison of solutal mixing and direct solute transfer

		$\mathrm{Ra} = 5 \times 10^3$		
Ha	$M_{\min}$	% change in $M_{\min}$	$M_{\max}$	% change in $M_{\max}$
0	−2.481		4.946	
2	−2.441	1.61	4.918	0.57
4	−2.329	4.59	4.836	1.67
8	−1.979	15.03	4.547	5.98
		$\mathrm{Ra} = 5 \times 10^4$		
0	−4.478		10.012	
2	−4.445	0.74	9.992	0.20
4	−4.349	2.16	9.932	0.59
8	−4.018	7.61	9.707	2.27

4.1. Overall heat and mass transfer

The average Nusselt and average Sherwood numbers are used to represent overall heat and mass transfers, and are denoted by $\mathrm{Nu}_{\mathrm{avg}}$ and $\mathrm{Sh}_{\mathrm{avg}}$, respectively. Table 3 compares overall heat and mass transfer for different Rayleigh (Ra) and Hartmann (Ha) numbers, respectively. It can be seen that when Ra increases from 5×10^3 to 5×10^4, the overall heat and mass transfer doubles, or there is a 100% increment. It is also worth noting that the Hartmann number (Ha) is more effective for lower Ra than for higher Ra. For higher Hartmann $(\mathrm{Ha} = 8)$, there is a maximum reduction in overall heat and mass transfer.

Table 3. Comparison of overall heat and mass transfer

		$\mathrm{Ra} = 5 \times 10^3$		
Ha	$\mathrm{Nu}_{\mathrm{avg}}$	% change in $\mathrm{Nu}_{\mathrm{avg}}$	$\mathrm{Sh}_{\mathrm{avg}}$	% change in $\mathrm{Sh}_{\mathrm{avg}}$
0	4.962		4.953	
2	4.934	0.57	4.925	0.57
4	4.852	1.66	4.843	1.66
8	4.562	5.99	4.553	5.99
		$\mathrm{Ra} = 5 \times 10^4$		
0	10.077		10.026	
2	10.057	0.20	10.006	0.20
4	9.997	0.59	9.947	0.59
8	9.770	2.28	9.721	2.27

5. Concluding remarks

The current research focuses on employing heat and mass lines approaches to visualize the heat and mass flows in MHD thermo-diffusion convection in an enclosure. Heat and mass flows inside the enclosure are best understood using heat and mass lines visualization techniques over isotherms and isoconcentrations. Overall, because of the dominance of buoyant force over viscous force as the Rayleigh number rises, heat and mass transmission from higher temperature and concentration walls to the fluid improves. Even a minor increase in the Hartmann number Ha results in a significant reduction in overall heat and mass fluxes. Furthermore, the reduction for smaller Rayleigh numbers Ra outweighs the reduction for larger Rayleigh numbers Ra. The largest reduction in overall heat and mass transport has been observed for greater Hartmann $(\mathrm{Ha} = 8)$. As a result, we can control heat and mass transfer by applying proper magnetic field strength.

References

[1] Mahapatra, T.R., Pal, D., & Mondal, S. (2013). Effects of buoyancy ratio on double-diffusive natural convection in a lid-driven cavity. *International Journal of Heat and Mass Transfer*, 57(2), 771-785.

[2] Corcione, M., Grignaffini, S., & Quintino, A. (2015). Correlations for the double-diffusive natural convection in square enclosures induced by opposite temperature and concentration gradients. *International Journal of Heat and Mass Transfer*, *81*, 811-819.

[3] He, B., Lu, S., Gao, D., Chen, W., & Li, X. (2019). Lattice Boltzmann simulation of double diffusive natural convection of nanofluids in an enclosure with heat conducting partitions and sinusoidal boundary conditions. *International Journal of Mechanical Sciences*, 161-162, 105003.

[4] Kefayati, G.H.R. (2019). Thermosolutal natural convection of viscoplastic fluids in an open porous cavity. *International Journal of Heat and Mass Transfer*, *138*, 401-419.

[5] Bondareva, N.S., Sheremet, M.A., Oztop, H.F., & Abu-Hamdeh, N. (2017). Heatline visualization of natural convection in a thick walled open cavity filled with a nanofluid. *International Journal of Heat and Mass Transfer*, *109*, 175-186.

[6] Hu, J.-T., Ren, X.-H., Liu, D., Zhao, F.-Y., & Wang, H.-Q. (2017). Natural convective heat and moisture transfer in an inclined building enclosure with one slender wall of finite thickness: Analytical investigation and non-unique Steady Flow Solutions. *International Journal of Heat and Mass Transfer*, *104*, 1160-1176.

[7] Kushawaha, D., Yadav, S., & Singh, D.K. (2020). Thermo-solute natural convection with heat and mass lines in a uniformly heated and soluted rectangular enclosure for low Prandtl number fluids. *International Journal of Thermal Sciences*, *148*, 106160.

[8] Khan, S.A., Hayat, T., Alsaedi, A., & Ahmad, B. (2021). Melting heat transportation in radiative flow of nanomaterials with irreversibility analysis. *Renewable and Sustainable Energy Reviews*, *140*, 110739.

[9] Hayat, T., Khan, S.A., & Alsaedi, A. (2021). Irreversibility characterization in nanoliquid flow with velocity slip and dissipation by a stretchable cylinder. *Alexandria Engineering Journal*, *60*(3), 2835-2844.

[10] Khan, M., Ahmad, L., Yasir, M., & Ahmed, J. (2021). Numerical Analysis in thermally radiative stagnation point flow of cross nanofluid due to shrinking surface: Dual solutions. *Applied Nanoscience*.

[11] Khan, S.A., Hayat, T., Ijaz Khan, M., & Alsaedi, A. (2020). Salient features of Dufour and Soret effect in radiative MHD flow of viscous fluid by a rotating cone with entropy generation. *International Journal of Hydrogen Energy*, *45*(28), 14552-14564.

[12] Ahmad, L., Ahmed, J., Khan, M., Yasir, M., & Alghamdi, M. (2020). Effectiveness of cattaneo–christov double diffusion in Sisko fluid flow with variable properties: Dual solutions. *Journal of Thermal Analysis and Calorimetry*, *143*(5), 3643-3654.

[13] Khan, S. A., Hayat, T., & Alsaedi, A. (2020). Entropy optimization in passive and active flow of liquid hydrogen based nanoliquid transport by a curved stretching sheet. *International Communications in Heat and Mass Transfer*, *119*, 104890.

[14] Hayat, T., Khan, S. A., Alsaedi, A., & Zai, Q. M. Z. (2020). Computational analysis of heat transfer in mixed convective flow of CNTS with entropy optimization by a curved stretching sheet. *International Communications in Heat and Mass Transfer*, *118*, 104881.

[15] Khan, S.A., Saeed, T., Khan, M.I., Hayat, T., Khan, M.I., & Alsaedi, A. (2019). Entropy optimized CNTS based Darcy-Forchheimer nanomaterial flow between two stretchable rotating disks. *International Journal of Hydrogen Energy*, *44*(59), 31579-31592.

[16] Hayat, T., Khan, S.A., & Alsaedi, A. (2020). Simulation and modeling of entropy optimized MHD flow of second grade fluid with dissipation effect. *Journal of Materials Research and Technology*, *9*(5), 11993-12006.

[17] Groşan, T., Sheremet, M.A., Pop, I., & Pop, S.R. (2018). Double-diffusive natural convection in a differentially heated wavy cavity under thermophoresis effect. *Journal of Thermophysics and Heat Transfer*, *32*(4), 1045-1058.

[18] Oztop, H.F., Mobedi, M., Abu-Nada, E., & Pop, I. (2012). A heatline analysis of natural convection in a square inclined enclosure filled with a CuO nanofluid under non-uniform wall heating condition. *International Journal of Heat and Mass Transfer*, *55*(19-20), 5076-5086.

[19] Kimura, S., & Bejan, A. (1983). The ”heatline” visualization of convective heat transfer. *Journal of Heat Transfer*, *105*(4), 916-919.

[20] Costa, V.A.F. (1997). Double diffusive natural convection in a square enclosure with heat and mass diffusive walls. *International Journal of Heat and Mass Transfer*, *40*(17), 4061-4071.

[21] Trevisan, O.V., & Bejan, A. (1987). Combined heat and mass transfer by natural convection in a vertical enclosure. *Journal of Heat Transfer*, *109*(1), 104-112.